Topotactic Engineering of Ultrathin 2D Nonlayered Nickel Selenides for Full Water Electrolysis

Hao Wu, Xin Lu, Gengfeng Zheng,* and Ghim Wei Ho*

Fabrication of ultrathin 2D nonlayered nanomaterials remains challenging, yet significant due to the new promises in electrochemical functionalities. However, current strategies are largely restricted to intrinsically layered materials. Herein, a combinatorial self-regulating acid etching and topotactic transformation strategy is developed to unprecedentedly prepare vertically stacked ultrathin 2D nonlayered nickel selenide nanosheets. Due to the inhibited hydrolyzation under acidic conditions, the self-regulating acid etching results in ultrathin layered nickel hydroxides (two layers). The ultrathin structure allows limited epitaxial extension during selenization, i.e., the nondestructive topotactic transformation, enabling facile artificial engineering of hydroxide foundation frameworks into ultrathin nonlayered selenides. Consequently, the exquisite nonlayered nickel selenide affords high turnover frequencies, electrochemical surface areas, exchange current densities, and low Tafel slopes, as well as facilitating charge transfer toward both oxygen and hydrogen evolution reactions. Thus, the kinetically favorable bifunctional electrocatalyst delivers advanced and robust overall water splitting activities in alkaline intermediates. The integrated methodology may open up a new pathway for designing other highly active 2D nonlayered electrocatalysts.

1. Introduction

Ultrathin 2D nanomaterials have been studied intensively in electrocatalysis because of their ultrahigh specific surface area and superior conductivity compared with the thick and

Dr. H. Wu, X. Lu, Prof. G. W. Ho
Department of Electrical and Computer Engineering
National University of Singapore
4 Engineering Drive 3, Singapore 117583, Singapore
E-mail: elehgw@nus.edu.sg

Prof. G. Zheng
Lab of Advanced Materials
Department of Chemistry
Fudan University
Shanghai 200433, China
E-mail: gfzheng@fudan.edu.cn

Prof. G. W. Ho
Engineering Science Programme
National University of Singapore
9 Engineering Drive 1, Singapore 117575, Singapore

Prof. G. W. Ho
Institute of Materials Research and Engineering
A*STAR (Agency for Science, Technology and Research)
3 Research Link, Singapore 117602, Singapore

The ORCID identification number(s) for the author(s) of this article can be found under https://doi.org/10.1002/aenm.201702704.

bulky counterparts.[1–11] In particular, 2D nonlayered materials are expected to show intriguing properties, as their surfaces are occupied with dangling bonds, unlike the layered materials.[12–15] The 3D atomic bonding in an unconventional dimensionality enables chemically active surface, thus reinforcing the catalytic capability.[16,17] Nickel selenides ($NiSe_2$ and $NiSe$), as nonlayered metal chalcogenides, have emerged as promising catalysts for water electrolysis, due to their favorable electrochemical reactivity toward both oxygen evolution reaction (OER) and hydrogen evolution reaction (HER).[18–24] Thus, integrating overall water splitting based on the low-cost ultrathin 2D nonlayered nickel selenide electrocatalysts, especially in alkaline intermediates for submissive industrial requirements, is promising. Unfortunately, engineering ultrathin 2D nonlayered nickel selenide is considerably challenging and rare, due to its intrinsic lack of anisotropic growth driving force of the nonlayered structure.[14–17]

Although epitaxial growth of 2D nonlayered nickel selenide has been achieved in-between ZnSe film and Ni foil very recently,[25] the rigorous requirements (lattice-matched substrate, high temperature, and vacuum), poor thickness controllability (over tens of nanometers), and limited surface area (parallel to the planar substrate) make it a suboptimal strategy. Other than that, composition transition through postselenization of the as-prepared precursors (e.g., nickel hydroxides, $Ni(OH)_2$) provides new possibilities for achieving nanostructured nickel selenides.[26–34] Yet, the structural deformation is inevitable during the selenization process due to the collective lattice expansion of individual layers (e.g., ≈58% increment in volume per unit cell as hexagonal $Ni(OH)_2$ converts to hexagonal NiSe) and crystal phase transformation, leading to the formation of nanoparticles or deformed thick sheet structures. In comparison, ultrathin 2D structures may render a well-retained structural framework in view of topotactic reaction on the surfaces that induces limited epitaxial lattice expansion and swelling of a few monolayer thick structure.[6,35–39] Thus, ultrathin 2D nonlayered nickel selenide is expected to be conceptualized, originating from the ultrathin layered $Ni(OH)_2$ counterparts. However, conventional synthetic protocols of $Ni(OH)_2$ under alkaline conditions practically result in thick sheets due to the fast and insubordinate hydrolysis

of Ni salts.[40] Moreover, exfoliation of bulky counterparts and bottom-up self-assembly introduces undesired intercalator/surfactant impurities, which would affect the topotactic selenization and dramatically hinder the exposed active sites for electrochemical reactions.[4,5,41–43] Theoretically, $Ni(OH)_2$ begins to precipitate when $[Ni^{2+}] \times [OH^-]^2 \geq K_{sp}$ (solubility product constant), according to the hydrolysis/dissociation reactions $(Ni^{2+} + 2H_2O \leftrightarrow Ni(OH)_2 \downarrow + 2H^+)$. Accordingly, it is calculated that the pH value of the growth media can be low as ≈3 to allow the formation of $Ni(OH)_2$ precipitates, where extensive dissociation would undergo under such acidic conditions to reach dynamic equilibrium. Hence, unlike the traditional alkaline media, it is expected to form thickness-constricted hydrolyzates in the acidic system, owing to the inhibited hydrolyzation. Therefore, the development of an effective and scalable approach via pH-controlled hydrolysis for the fabrication of ultrathin and well-assembled 2D nonlayered structures is paramount for electrocatalysis.

Herein, we propose a self-limiting tunable acid etching to prepare hierarchical ultrathin (≈0.96 nm) 2D layered $Ni(OH)_2$ nanosheets, followed by an artificial topotactic phase engineering into ultrathin (≈1.25 nm) nonlayered NiSe nanosheets, as schematically shown in **Figure 1**a. With the pH self-regulation, in situ etching of Ni foam that simultaneously serves as Ni ion sources and support lends to superior interfacial contact,

leading to two-tiered interlaced ultrathin nanosheet structures. Significantly, unlike the bulky structures that succumb to excessive lattice expansion owing to their thick dimensionality, the elaborate ultrathin layered frameworks allow nondestructive topotactic selenization to readily transform into nonlayered counterparts. Notably, no studies focusing on such facile combinative synthetic strategies are established thus far, to acquire ultrathin and tiered 2D nonlayered NiSe nanosheets. With this established methodology, highly efficient and stable OER and HER electrodes with low Tafel slopes and onset potentials as well as high current densities are achieved in alkaline intermediates. The electrocatalytic overall water splitting performance, based on the bifunctional ultrathin nonlayered NiSe nanosheets, shows superiority to the layered hydroxide counterparts achieved by acid etching and also hydrothermal reaction in alkaline media. The proposed simple yet competent strategy that exploits combinatorial self-regulated acid etching and topotactic phase transformation sheds light on engineering of other ultrathin 2D nonlayered nanoframeworks.

2. Results and Discussion

A plausible formation mechanism (Figure 1b) of hierarchical two-tiered nickel hydroxide nanosheets is proposed, of which
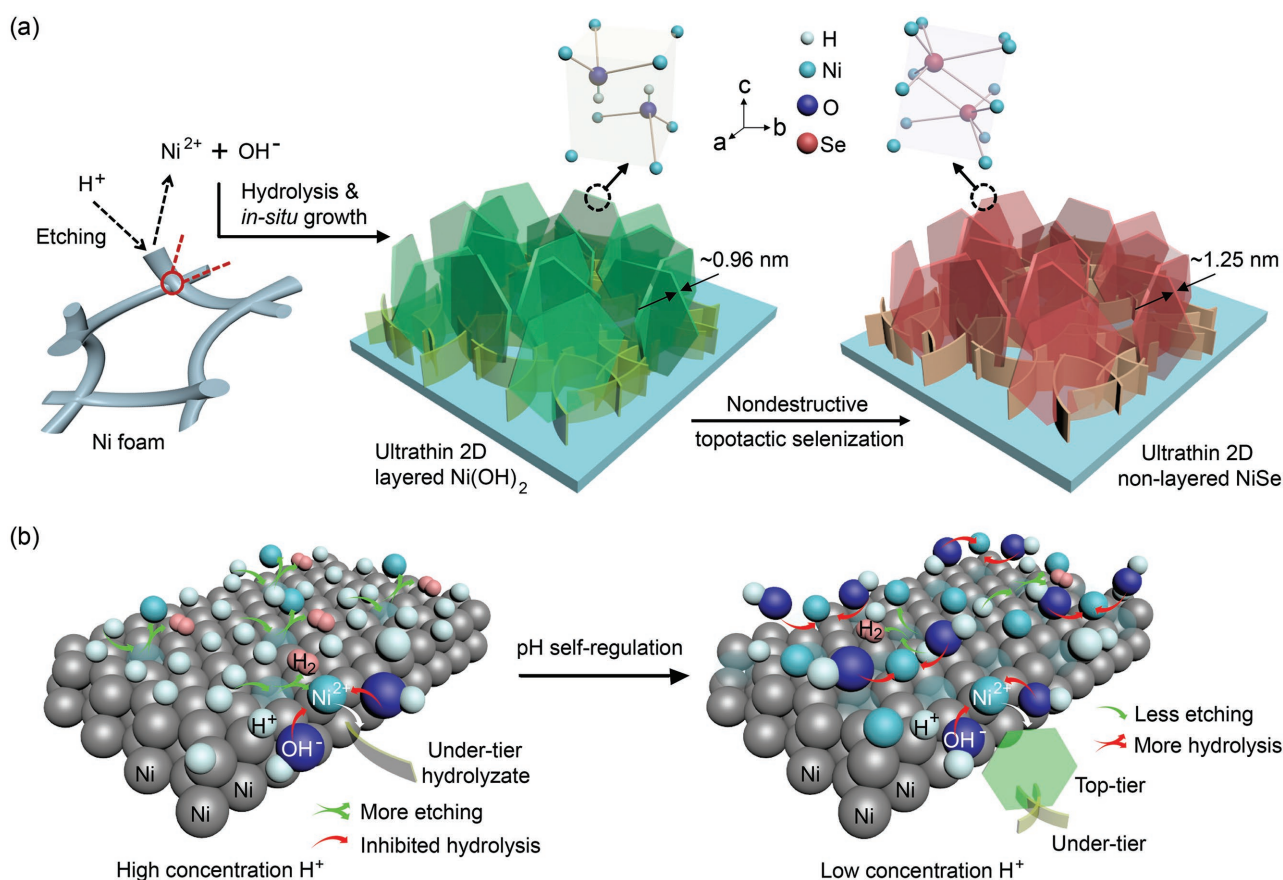

Figure 1. a) Structural evolution of ultrathin 2D layered $Ni(OH)_2$ nanosheets and ultrathin 2D nonlayered NiSe nanosheets through combinatorial acid etching and topotactic selenization. b) Schematic illustration of two-tiered nanosheet formation via in situ self-regulating acid etching.

the corresponding reaction equations are addressed in the Supporting Information. At the initial stage, Ni atoms on the surface are etched under high concentration of H^+ (pH ≈ 3.7) to form Ni^{2+} ions, where only trace amount of them would undergo hydrolyzation to form restrictive basal nanostructured nickel hydroxides. With the consumption of H^+ ions (pH ≈ 6), more Ni^{2+} ions are accessible to hydrolyze, resulting in the formation of nickel hydroxide nanosheets with a relatively large size but still low thickness due to dissociation under acidic conditions. Hence, two-tiered hydrolyzates with interconnected ultrathin nanosheets are formed in a one-step process.

A uniform network composed of ultrathin nanosheets is clearly shown for the H^+ etched sample by typical optical and scanning electron microscope (SEM) images (**Figure 2**a,b; Figures S1 and S2, Supporting Information). Interestingly, two-tiered interwoven ultrathin nanosheets with discrepant sizes are observed (Figure 2c), manifesting the successful formation of hierarchical nonsymmetrical porous structures through the one-step in situ acid etching methodology. The morphology evolution of the hydrolyzates was recorded with the etching times of 2, 4, and 20 h (Figure 2a; Figure S3, Supporting Information). Only one-layered nanosheet was formed after being etched for 2 h, and sparse nanosheets appeared above the bottom-tiered nanosheets after 4 h, which became a dense layer that covered the whole surface after 20 h. The morphology evolution provides reliable evidence for the formation of two-tiered nanosheet structure. Moreover, the two-tiered nanosheet

structure is observed in the case of Co foam etching (Figure S4, Supporting Information), demonstrating the rationality of the proposed formation mechanism and universality of the self-regulating acid etching strategy. The average size of top-tiered nanosheets is ≈ 1 µm, while it ≈ 200 nm for the bottom tiers (Figure S5, Supporting Information). Notably, the top-tiered nanosheets are intimately interfaced with the underlying tier (Figure S6, Supporting Information), owing to the one-pot sequential hydrolysis reactions and well-matched lattice constant of the homophase nanosheets. Transmission electron microscope (TEM) image of the H^+ etched sample shows an ultrathin 2D nanosheet feature (Figure S7, Supporting Information), and the corresponding selected area electron diffraction (SAED) pattern reveals the single-crystal characteristic of the individual nanosheet (Figure 2d). The observed lattice fringe with an interplanar spacing of ≈ 0.23 nm shown in Figure 2e is consistent with the (101) plane of hexagonal β-$Ni(OH)_2$. As expected, the ultrathin nanosheet structure is well retained after a selenization treatment as shown in SEM images (Figure 2f; Figure S8, Supporting Information) and the typical TEM image (Figure S9, Supporting Information). The SAED pattern (inset of Figure 2g) indicates the single-crystal nature of the nanosheet, and typical lattice fringes (Figure 2g) with the spacing of ≈ 0.21 and 0.15 nm are matched with (102) and (201) planes of hexagonal NiSe, respectively. A typical elemental mapping shows the homogeneous dispersion of Ni and Se elements with a ratio of $\approx 1:1$ (Figure S10, Supporting Information) in the
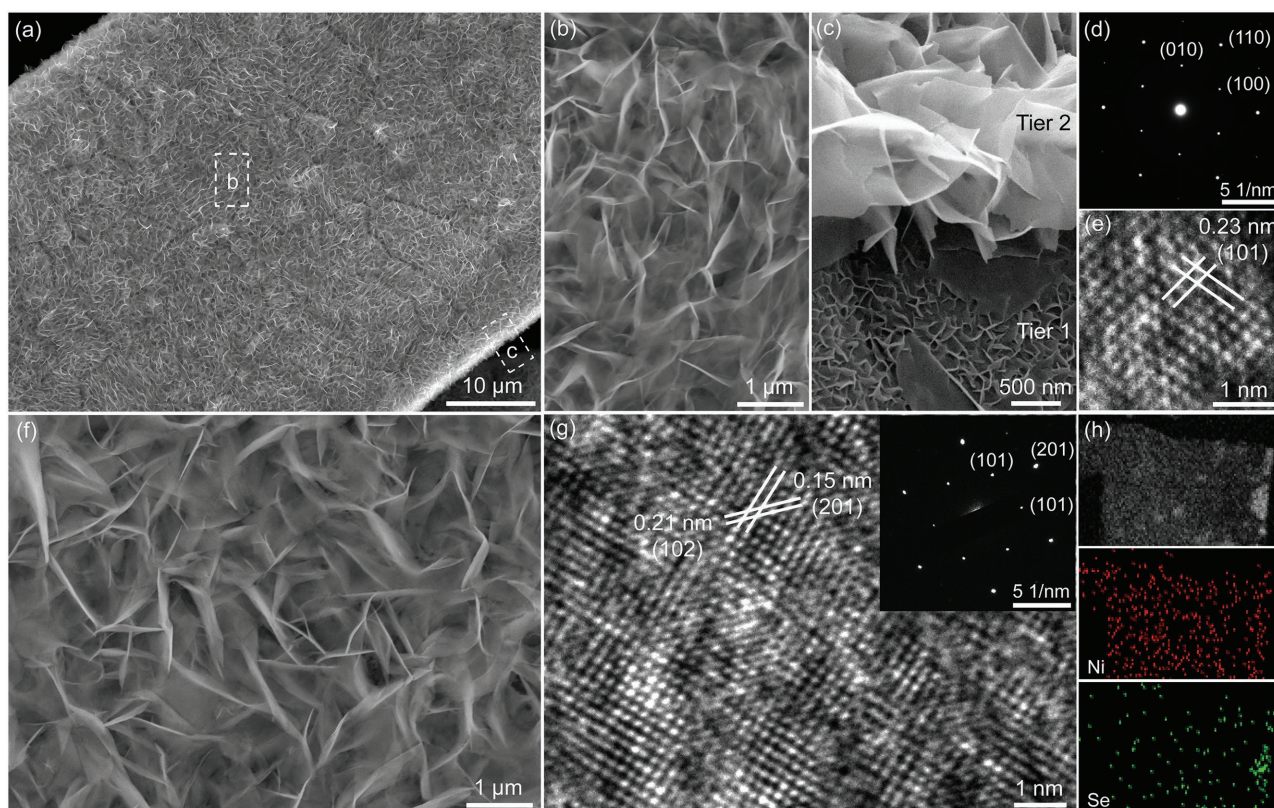

Figure 2. a) SEM image of ultrathin $Ni(OH)_2$ nanosheets. b,c) High-magnification SEM images of ultrathin two-tiered $Ni(OH)_2$ nanosheets. d) SAED pattern of ultrathin $Ni(OH)_2$ nanosheets. e) TEM image of ultrathin $Ni(OH)_2$ nanosheets. f) SEM image of ultrathin NiSe nanosheets. g) HRTEM image of ultrathin NiSe nanosheets. Inset: Corresponding SAED pattern. h) TEM image of ultrathin NiSe nanosheet and corresponding elemental mapping.

ultrathin NiSe nanosheet (Figure 2h), revealing the success of the phase transformation.

X-ray diffraction (XRD) characterization was performed to further identify the stoichiometric proportion of the acid-etched nanosheets and the subsequent selenides (**Figure 3**a). Besides the diffraction peaks of Ni foam, all remaining peaks of the H+ etched sample are matched with pure hexagonal β-Ni(OH)$_2$ (PDF no. 14-0117),[44] which is consistent with the TEM results. After selenization, all newly emerged diffraction peaks belong to pure hexagonal NiSe (PDF no. 02-0892),[45] while previous peaks of β-Ni(OH)$_2$ disappear, indicating the complete phase conversion. Atomic force microscope (AFM) was used to reveal the thickness of nanosheets before and after selenization (Figure 3b,c). As can be seen, both the nanosheets show uniform thicknesses, of which the value of ≈0.96 nm for β-Ni(OH)$_2$ reveals that the nanosheets are composed of only two layers (unit cell, $a = b = 3.12$ Å, $c = 4.66$ Å).[46] The increment of thickness after selenization is attributed to the structure transformation (layered to nonlayered) and lattice expansion from β-Ni(OH)$_2$ to NiSe (unit cell, $a = b = 3.66$ Å, $c = 5.33$ Å).[45] In contrast, Ni(OH)$_2$ nanosheets synthesized via the hydrothermal method[40] manifest only a single-tiered nanosheet structure (Figure S11, Supporting Information) with a much larger

lateral size and thickness (≈4 µm and 50–100 nm, respectively). A severe structural deformation is observed for the hydrothermal thick nanosheets, demonstrating the advancement of ultrathin ones on structural retention during phase transformation (Figure S12, Supporting Information). Thanks to the ultrathin nature of the nanosheets, the as-obtained 2D nanosheets allow a nondestructive topotactic selenization, leading to the formation of ultrathin 2D selenides with the morphology well retained. X-ray photoelectron spectroscopy (XPS) spectra were then detected to confirm the valence state of the elements. Two sets of typical 2p peaks of Ni^{2+} (873.3 and 855.2 eV) and the deconvoluted O^{2-} and OH$^-$ (530.8 and 531.6 eV) of O 1s[20,47] further verify the formation of Ni(OH)$_2$ in the one-step acid etching (Figure S13, Supporting Information). The Ni retains bivalence after selenization (Figure 3d), while the deconvoluted peaks located at 54.9 and 54.4 eV match with the 3d$_{3/2}$ and 3d$_{5/3}$ of Se^{2-}, respectively,[23] indicating the formation of NiSe (Figure 3e). The small peak centered at 58.2 eV corresponds to the surface oxidation of NiSe.[18,20,23]

The OER behaviors, including linear sweep voltammetry (LSV) curves and relative Tafel plots, are exhibited for the hierarchical ultrathin 2D nonlayered NiSe, layered Ni(OH)$_2$, and hydrothermal Ni(OH)$_2$ nanosheets (denoted as two-tiered
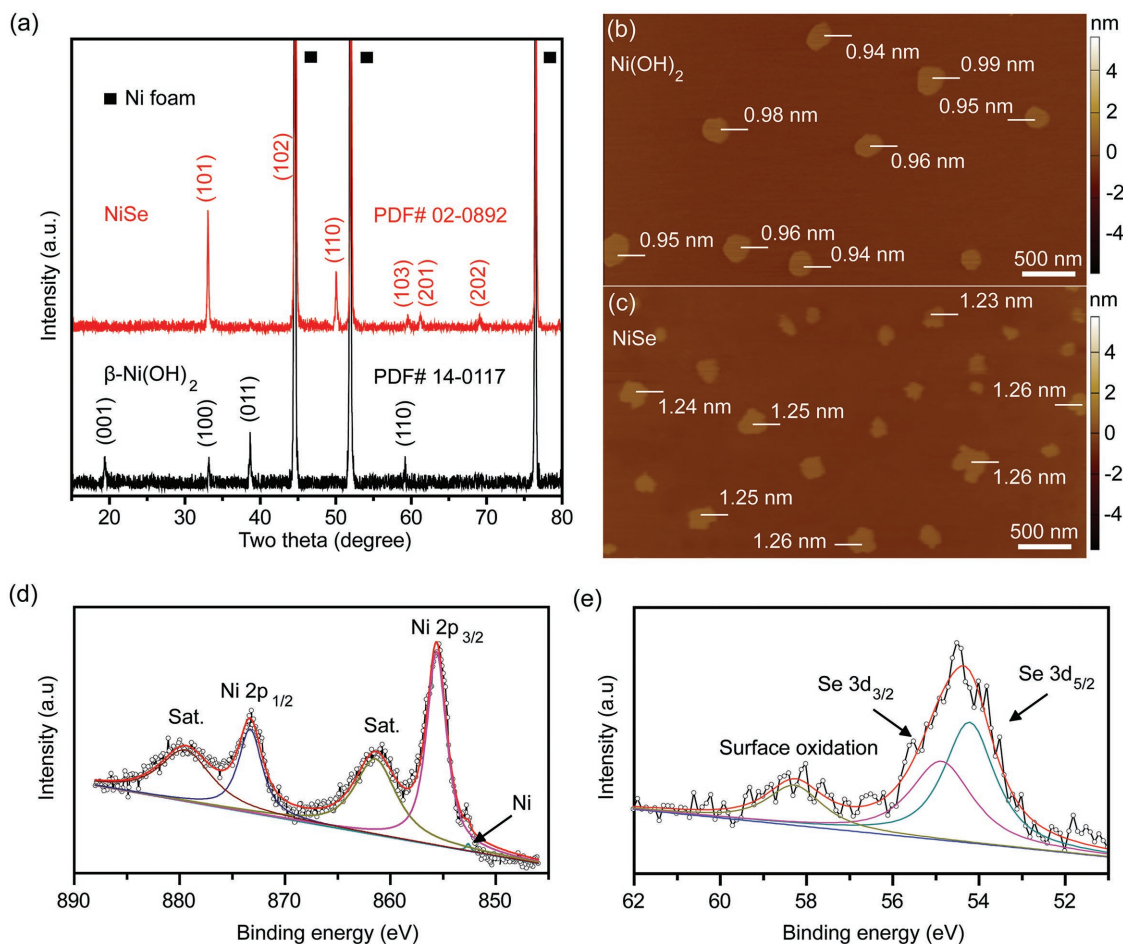

Figure 3. a) XRD pattern of ultrathin NiSe and Ni(OH)$_2$ nanosheets. b,c) AFM images of ultrathin NiSe and Ni(OH)$_2$ nanosheets, respectively. d,e) XPS Ni 2p and Se 3d spectra of ultrathin NiSe nanosheets, respectively.
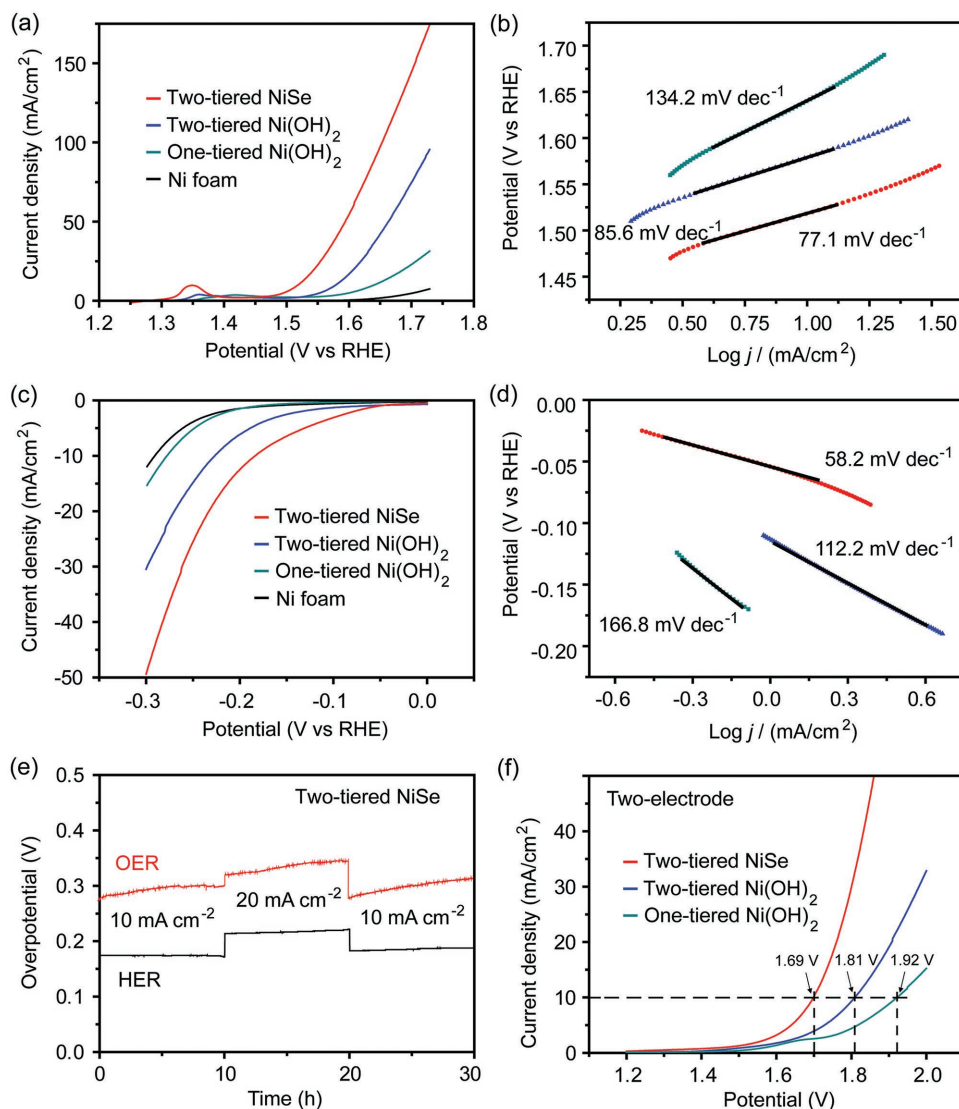
Figure 4. a) OER LSV curves of ultrathin two-tiered NiSe, two-tiered $Ni(OH)_2$, one-tiered $Ni(OH)_2$ nanosheets, and bare Ni foam. b) Corresponding Tafel plots. c) HER LSV curves of ultrathin two-tiered NiSe, two-tiered $Ni(OH)_2$, one-tiered $Ni(OH)_2$ nanosheets, and bare Ni foam. d) Corresponding Tafel plots. e) Galvanostatic OER and HER stability test of two-tiered NiSe nanosheets. f) Two-electrode LSV curves.

NiSe, two-tiered $Ni(OH)_2$, and one-tiered $Ni(OH)_2$, respectively). Impressively, the ultrathin two-tiered $Ni(OH)_2$ electrode shows a much lower overpotential of 350 mV compared with the thick one-tiered $Ni(OH)_2$ nanosheet (410 mV), indicating the superiority of the ultrathin two-tiered structure, as shown in **Figure 4**a. With selenization evolution, the ultrathin 2D nonlayered two-tiered NiSe decreases the overpotential to 290 mV to deliver a current density of 10 mA cm^{-2} for OER activity, indicating a higher OER activity. The current density of two-tiered NiSe at 1.70 V versus RHE can be reached to 144.5 mA cm^{-2}, which is almost twofold of the two-tiered $Ni(OH)_2$ (74.6 mA cm^{-2}) and 5.3 times higher than that of the one-tiered $Ni(OH)_2$ electrode (22.9 mA cm^{-2}), while the Ni foam substrate contributes negligibly to the OER activity (4.7 mA cm^{-2} at 1.70 V). Accordingly, the Tafel slope of two-tiered NiSe is as low as 77.1 mV decade^{-1} (Figure 4b), which is smaller than that of the two-tiered $Ni(OH)_2$ (85.6 mV decade^{-1}) and much smaller than

the one-tiered $Ni(OH)_2$ (134.2 mV decade^{-1}), revealing the fast OER kinetics of the ultrathin two-tiered NiSe nanosheets. The oxidation humps at ≈1.35 and ≈1.36 V for the two-tiered NiSe and two-tiered $Ni(OH)_2$ electrodes are ascribed to the oxidation of Ni(II) to Ni(III), while the one-tiered β-$Ni(OH)_2$ shows a much weaker and broader oxidation hump at a more positive potential (≈1.42 V), which can be attributed to a higher mass loading and poor electric conductivity.[23,26] Notably, to exclude the inaccuracy of the reference electrode and the effect of ion (e.g., Fe^{3+}) impurity of the electrolyte for OER, LSV curves were determined further with Hg/HgO as the reference electrode and with purified electrolyte, respectively (Figure S14, Supporting Information). The curves show negligible difference with either the Hg/HgO reference electrode or the purified electrolyte compared with those with the Ag/AgCl reference electrode or the untreated electrolyte, indicating the reliable OER performances of all electrodes.

ADVANCED
SCIENCE NEWS
www.advancedsciencenews.com

ADVANCED
ENERGY
MATERIALS
www.advenergymat.de

On the other hand, the HER performances are evaluated for all three samples, as shown in Figure 4c,d. Distinctly, the ultrathin two-tiered NiSe displays the lowest overpotential of 177 mV at 10 mA cm^{-2}, which is much lower than that of the two-tiered Ni(OH)$_2$ (230 mV) and one-tiered Ni(OH)$_2$ (278 mV) electrodes (Figure 4c). The current density at −0.25 V versus RHE for two-tiered NiSe is 28.9 mA cm^{-2}, which is about 2- and 5.6-fold of the two-tiered Ni(OH)$_2$ and one-tiered Ni(OH)$_2$ electrodes (14.3 and 5.2 mA cm^{-2}), respectively. The corresponding Tafel slope of the two-tiered NiSe is as low as 58.2 mV decade^{-1} (Figure 4d), much better than the other two electrodes (112.2 and 166.8 mV decade^{-1}). Unambiguously, the HER kinetics of the ultrathin nanosheets overwhelms the thicker ones, while the nonlayered NiSe shows superiority to the layered Ni(OH)$_2$ nanosheets. Moreover, both OER and HER stability behaviors of the highly active ultrathin nonlayered NiSe electrodes are evaluated under galvanostatic mode with a multicurrent step for 30 h, as shown in Figure 4e. The increments of overpotential for OER and HER after the consecutive operation are only about 16% (270–315 mV) and 7% (173–185 mV), respectively, indicating the sturdy durability performed in alkaline media. The morphologies of the electrodes after OER and HER tests are both well maintained, indicating the robust structure of the electrode, as shown in the SEM images (Figure S15, Supporting Information). XPS spectra after the OER stability test (Figure S16, Supporting Information) show the appearance of Ni^{3+} (856.3 eV) and O^{2-} (531 eV) peaks that originated from the oxidation surfaces in the form of NiOOH, which were commonly observed in metal chalcogenides during the OER catalytic process.[23] There is no apparent decrease in the Se 3d signal, suggesting the robustness of the surface composition of ultrathin NiSe.[48] The characteristic peaks of both Ni and Se have negligible changes after the HER test, revealing the stable behavior for the consecutive operation in alkaline media (Figure S17, Supporting Information). As the nanosheets exhibit stable activities toward both OER and HER, the overall water splitting evaluation is thus performed based on the bifunctional catalysts with a two-electrode mode, as shown in Figure 4f. To deliver a current density of 10 mA cm^{-2}, the potential needed for ultrathin 2D nonlayered NiSe is 1.69 V, which is much smaller than those based on layered two-tiered Ni(OH)$_2$ (1.81 V) and one-tiered Ni(OH)$_2$ (1.92 V), demonstrating the great potential for advanced alkaline water electrolysis.

To detect the overall water splitting behavior in a more practical application, a drainage system is adopted for collecting the gases (Figure S18, Supporting Information). With a current density of 40 mA cm^{-2} reached at ≈2.1 V (Figure S19, Supporting Information), the amount of H$_2$ and O$_2$ constantly evolves in stoichiometric proportion of 2:1 (**Figure 5**a). The acquisition of 10 mL H$_2$ is realized within ≈35.6 min (corresponding to an H$_2$ production rate of ≈0.75 mmol h^{-1}) with a Faradaic efficiency of nearly 100%. To uncover the intrinsically high OER and HER activities of the ultrathin 2D nonlayered NiSe, turnover frequencies (TOFs), quantifying the specific activity of catalytic reactions,[27,28] are calculated and compared among the three samples (Figure 5b,c). As estimated, the TOF of two-tiered NiSe nanosheets for OER at 1.7 V versus RHE is 1.87 s^{-1}, which is almost 2-fold

of two-tiered Ni(OH)$_2$ and 14.6 times higher than that of the hydrothermal one-tiered Ni(OH)$_2$ electrode (0.12 s^{-1}). Meanwhile, the two-tiered NiSe nanosheet for HER shows a TOF of 0.75 s^{-1} at −0.25 V, which is about 2-fold of the two-tiered Ni(OH)$_2$ and 15-fold of the one-tiered Ni(OH)$_2$. The predominant TOFs of the ultrathin two-tiered NiSe nanosheet are responsible for the high activity as both OER and HER catalysts. Other than TOF, the electrochemical double-layer capacitance-derived surface area (ECSA) is another convincing factor that can be used to estimate the accessible active sites for the electrodes (Figures S20 and S21, Supporting Information).[26,27] Markedly, the two-tiered NiSe nanosheets display high ECSAs of 32.8 and 33.8 mF cm^{-2} for OER and HER, respectively, which are much larger than those of the other two electrodes (16.6 and 13.2 mF cm^{-2} for two-tiered Ni(OH)$_2$ and 5.4 and 1.6 mF cm^{-2} for one-tiered Ni(OH)$_2$, respectively). The overwhelmingly high ECSAs endow vast active sites while the high TOFs enable them highly reactive, thus ensuring highly efficient electrocatalytic abilities of the ultrathin two-tiered NiSe nanosheets. The exchange current densities (j_0), revealing the inherent catalytic activity of the catalyst, were extracted by extrapolating the Tafel slopes.[20,27] A high j_0 of 18.7 μA cm^{-2} is achieved for the ultrathin two-tiered NiSe nanosheet in OER, which slightly surpasses the value of 17.4 μA cm^{-2} for two-tiered Ni(OH)$_2$ and greatly exceeds the value for the one-tiered Ni(OH)$_2$ electrode (11.2 μA cm^{-2}). An enhancement of j_0 is also observed in the HER catalytic process (1.11, 1.03, and 0.93 μA cm^{-2} for two-tiered NiSe, two-tiered Ni(OH)$_2$, and one-tiered Ni(OH)$_2$, respectively). The improved j_0 of NiSe nanosheets indicates the intrinsically advanced catalytic activities for water splitting.

Additionally, the resistance between the interfaces, affecting the charge transfer kinetics, is investigated with electrochemical impedance spectroscopy (EIS).[20–22,47] The Nyquist plots and corresponding equivalent circuits (Figure 5f and inset) of two-tiered NiSe for OER clearly present a low series resistance (R_s, 1.86 Ω) and two charge transfer resistances (R_{ct}, 0.13 and 0.06 Ω), similar to the two-tiered Ni(OH)$_2$ electrode (R_s, 2.24 Ω; R_{ct}, 0.11 and 0.05 Ω), indicating the high conductivity of the sturdy two-tiered structures. Notably, the appearance of the Gerischer impedance in the two-tiered electrodes confirms their highly porous nature.[47] As comparison, the hydrothermal one-tiered Ni(OH)$_2$ shows a larger R_s (2.46 Ω) and only one R_{ct} (0.21 Ω), matching the one-tiered structure (Figure S22a, Supporting Information). For the HER process, the two-tiered NiSe electrode shows the lowest R_s (1.85 Ω) and two R_{ct} (1.22 and 3.76 Ω) compared with the two-tiered Ni(OH)$_2$ electrode (R_s, 1.86 Ω; R_{ct}, 1.23 and 4.32 Ω) and the hydrothermal one-tiered Ni(OH)$_2$ electrode (R_s, 1.88 Ω; R_{ct}, 5.88 Ω), revealing a preferable charge transfer of the two-tiered NiSe structure (Figure 5g). Notably, only one semicircle is shown in the thick case, indicating that the surface is partially blocked during the catalytic process (Figure S22b, Supporting Information), and further demonstrating the superiority of the two-tiered ultrathin nanostructures for electrocatalytic reactions. Thus, high TOFs, large ECSAs, and enhanced conductivity of the ultrathin 2D nonlayered NiSe nanosheets contribute to the advanced OER and HER catalytic properties,
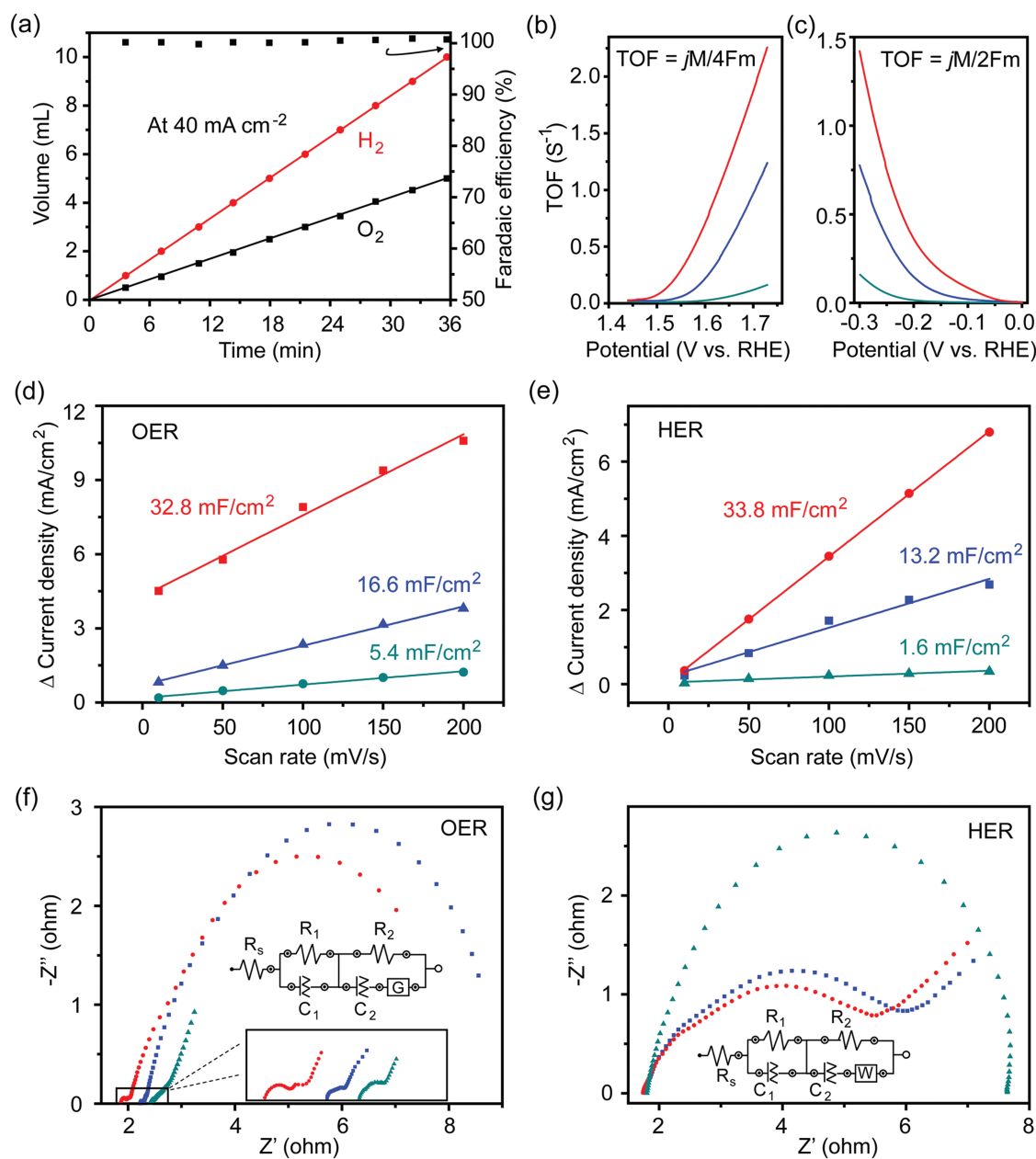
Figure 5. a) Two-electrode configuration based on two-tiered NiSe nanosheets for gas collection. b,c) TOF plots of OER and HER, respectively. d,e) ECSAs of OER and HER, respectively. f,g) Nyquist plots of OER and HER, respectively.

which are highly competitive to the benchmark transition metal selenide-based electrocatalysts (Table S1, Supporting Information).

3. Conclusion

In summary, a combinatorial self-regulated acidic etching and topotactic selenization methodology has been adopted to prepare ultrathin 2D nonlayered NiSe nanosheets. Elaborate two-tiered morphology is established unprecedentedly with

the tunable pH media, and intact transformation from layered nanosheets to the nonlayered counterparts is realized by topotactic selenization due to their ultrathin nature. With the newly established strategy, high TOFs, ECSAs, and j_0, as well as facilitated charge transfer toward both OER and HER, are achieved, thus leading to highly efficient and stable electrodes with low overpotentials, Tafel slopes, and high current densities in alkaline intermediates. The topotactic engineered ultrathin 2D nonlayered NiSe nanosheet electrodes show great potential for advanced electrocatalytic overall water splitting with a nearly 100% Faradaic efficiency. The proposed competent strategies

enlighten the engineering for other ultrathin 2D nonlayered nanoframeworks.

4. Experimental Section

Chemicals: HCl, $Ni(NO_3)_2\cdot6H_2O$, Se powder, $NaBH_4$, urea, NH_4F, and NaOH were purchased from Sigma-Aldrich. All reagents were used as received without further purification.

Synthesis of Ultrathin 2D Layered $Ni(OH)_2$ Nanosheets: To obtain hierarchically structured $Ni(OH)_2$ nanosheets, an in situ acidic wet etching method was developed. First, a piece of Ni foam (4 cm × 1 cm, or Co foam to obtain two-tiered $Co(OH)_2$ nanosheets) was immersed into 1 M HCl with ultrasonic treatment to wash away thoroughly the oxidation layer. Then, it was transferred to a sealed glass bottle with 0.2×10^{-3} M HCl aqueous solution (20 mL) and heated to 80 °C under stirring for 20 h. After that, the substrate was allowed to cool down to room temperature naturally and washed with deionized (DI) water, followed by a drying process in an air-flow oven at 50 °C.

Synthesis of Ultrathin 2D Nonlayered NiSe Nanosheets: For NiSe nanosheet fabrication, the as-prepared hierarchical ultrathin $Ni(OH)_2$ nanosheet was sealed in an autoclave and filled with 0.1×10^{-3} M NaHSe aqueous solution. NaHSe was obtained by fully mixing Se powder and $NaBH_4$ in a molecular ratio of 1:2 in DI water. The topotactic reaction was conducted with a hydrothermal treatment at 180 °C for 4 h. The sample was taken out and washed with ethanol and DI water thoroughly.

Synthesis of One-Tiered $Ni(OH)_2$ Nanosheets: For comparison, a typical hydrothermal method was adopted as in a previous work.[40] In detail, Ni foam was first treated with HCl for oxidation removal and then put into an autoclave with a mixture of 0.1 M $Ni(NO_3)_2\cdot6H_2O$, 0.5 M urea, and 0.2 M NH_4F. The hydrothermal process was conducted at 120 °C for 4 h, followed by washing with DI water and drying at 50 °C. For selenization, the as-prepared $Ni(OH)_2$ nanosheet underwent a similar hydrothermal treatment with the molecular ratio of $Ni(OH)_2$ to NaHSe of 1:1. After 4 h treatment at 180 °C, the sample was washed with ethanol and DI water thoroughly.

Characterization: SEM images were captured on a JEOL JSM-7001F field emission scanning electron microscope. High-resolution TEM (HRTEM) images, energy-dispersive X-ray spectroscopy (EDX) images, and elemental mapping images were recorded on a JEOL JEM-2100 electron microscope. The XRD patterns were obtained on a Philips X-ray diffractometer with Cu Kα radiation. Tapping-mode AFM measurements were performed on a commercial SPM instrument under AC mode in air (MPF-3D Stand Alone, Asylum Research, USA). XPS measurements were recorded on a Thermo Scientific ESCA Lab 250 spectrometer.

Electrochemical Measurements: All electrochemical measurements were performed in a CHI 660E electrochemical workstation. All as-prepared substrates were directly used as working electrodes and tailored to be 1 cm^2 in size. In a three-electrode configuration, a graphite rod and saturated calomel electrode (SCE) were used as the counter electrode and reference electrode, respectively. In a two-electrode mode, bifunctional $Ni(OH)_2$ samples were set as anode and cathode. All tests were conducted in 1 M aqueous NaOH electrolyte. The measured potential was calibrated to RHE according to the following equation: $E_{RHE} = E_{SCE} + 0.245\ V + 0.059 \times pH$. All polarization curves were recorded at a scanning rate of 1 mV s^{-1}, without *iR* compensation. Moreover, a Nafion membrane was used for blocking bubble diffusion during the gas collection process by a classical drainage method in the two-electrode mode. Notably, the gas collection operation started after 20 min of the galvanostatic test at 40 mA cm^{-2} to expel the air in the bottles and was recorded at every 1 mL of H_2 accumulation. The Faradaic efficiency was calculated by the formula $\eta = zn/Q$, where z, n, and Q represent the number of electrons transferred, the amount of substance, and the total power consumption, respectively. The turnover frequencies for OER and HER were estimated by the following equations: $TOF = jM/4Fm$ and $TOF = jM/2Fm$, where j is the current density, F is Faraday's constant (96 485.3 C mol^{-1}), M is the molar mass, m is the loading mass, and

numbers 4 and 2 mean 4 and 2 electrons per mole of O_2 and H_2, respectively.[27] The loading density of one-tiered $Ni(OH)_2$ nanosheet was ≈2.5 mg cm^{-2}, which was calculated by weighing the difference before and after the hydrothermal process. For the two-tiered $Ni(OH)_2$ and NiSe, the mass loadings were calculated by assuming that all HCl was used up, while all $Ni(OH)_2$ components were converted during the selenization process. The loading densities were estimated to be 0.46 and 0.69 mg cm^{-2}, respectively.

Supporting Information

Supporting Information is available from the Wiley Online Library or from the author.

Conflict of Interest

The authors declare no conflict of interest.

[1] M. Chhowalla, H. S. Shin, G. Eda, L. J. Li, K. P. Loh, H. Zhang, *Nat. Chem.* **2013**, *5*, 263.

[2] M. Q. Yang, Y. J. Xu, W. Lu, K. Zeng, H. Zhu, Q. H. Xu, G. W. Ho, *Nat. Commun.* **2017**, *8*, 14224.

[3] H. Yin, Z. Tang, *Chem. Soc. Rev.* **2016**, *45*, 4873.

[4] J. Feng, X. Sun, C. Wu, L. Peng, C. Lin, S. Hu, J. Yang, Y. Xie, *J. Am. Chem. Soc.* **2011**, *133*, 17832.

[5] Z. Sun, T. Liao, Y. Dou, S. M. Hwang, M. S. Park, L. Jiang, J. H. Kim, S. X. Dou, *Nat. Commun.* **2014**, *5*, 3813.

[6] X. Liu, R. Ma, Y. Bando, T. Sasaki, *Adv. Mater.* **2012**, *24*, 2148.

[7] P. Sun, R. Ma, X. Bai, K. Wang, H. Zhu, T. Sasaki, *Sci. Adv.* **2017**, *3*, e1602629.

[8] L. Zhu, W. L. Ong, X. Lu, K. Zeng, H. J. Fan, G. W. Ho, *Small* **2017**, *13*, 1700084.

[9] T. Y. Ma, J. L. Cao, M. Jaroniec, S. Z. Qiao, *Angew. Chem., Int. Ed.* **2016**, *55*, 1138.

[10] L. Cheng, W. Huang, Q. Gong, C. Liu, Z. Liu, Y. Li, H. Dai, *Angew. Chem., Int. Ed.* **2014**, *53*, 7860.

[11] W. Liu, E. Hu, H. Jiang, Y. Xiang, Z. Weng, M. Li, Q. Fan, X. Yu, E. I. Altman, H. Wang, *Nat. Commun.* **2016**, *7*, 10771.

ADVANCED
SCIENCE NEWS

www.advancedsciencenews.com

ADVANCED
ENERGY
MATERIALS

www.advenergymat.de

[12] T. Liu, D. Liu, F. Qu, D. Wang, L. Zhang, R. Ge, S. Hao, Y. Ma, G. Du, A. M. Asiri, L. Chen, X. Sun, *Adv. Energy Mater.* **2017**, *7*, 1700020.

[13] J. Hu, A. Liu, H. Jin, D. Ma, D. Yin, P. Lin, S. Wang, Z. Lin, J. Wang, *J. Am. Chem. Soc.* **2015**, *137*, 11004.

[14] C. Tan, H. Zhang, *Nat. Commun.* **2015**, *6*, 7873.

[15] F. Wang, Z. Wang, T. A. Shifa, Y. Wen, F. Wang, X. Zhan, Q. Wang, K. Xu, Y. Huang, L. Yin, C. Jiang, J. He, *Adv. Funct. Mater.* **2017**, *27*, 1603254.

[16] C. Tan, H. Zhang, *J. Am. Chem. Soc.* **2015**, *137*, 12162.

[17] W. Cheng, J. He, T. Yao, Z. Sun, Y. Jiang, Q. Liu, S. Jiang, F. Hu, Z. Xie, B. He, W. Yan, S. Wei, *J. Am. Chem. Soc.* **2014**, *136*, 10393.

[18] I. H. Kwak, H. S. Im, D. M. Jang, Y. W. Kim, K. Park, Y. R. Lim, E. H. Cha, J. Park, *ACS Appl. Mater. Interfaces* **2016**, *8*, 5327

[19] M.-R. Gao, Z.-Y. Lin, T.-T. Zhuang, J. Jiang, Y.-F. Xu, Y.-R. Zheng, S.-H. Yu, *J. Mater. Chem.* **2012**, *22*, 13662.

[20] F. Wang, Y. Li, T. A. Shifa, K. Liu, F. Wang, Z. Wang, P. Xu, Q. Wang, J. He, *Angew. Chem., Int. Ed.* **2016**, *55*, 6919.

[21] B. Yu, X. Wang, F. Qi, B. Zheng, J. He, J. Lin, W. Zhang, Y. Li, Y. Chen, *ACS Appl. Mater. Interfaces* **2017**, *9*, 7154.

[22] H. Zhou, Y. Wang, R. He, F. Yu, J. Sun, F. Wang, Y. Lan, Z. Ren, S. Chen, *Nano Energy* **2016**, *20*, 29.

[23] C. Tang, N. Cheng, Z. Pu, W. Xing, X. Sun, *Angew. Chem., Int. Ed.* **2015**, *54*, 9351.

[24] Z. Gao, J. Qi, M. Chen, W. Zhang, R. Cao, *Electrochim. Acta* **2017**, *224*, 412.

[25] C. Cai, Y. Ma, J. Jeon, F. Huang, F. Jia, S. Lai, Z. Xu, C. Wu, R. Zhao, Y. Hao, Y. Chen, S. Lee, M. Wang, *Adv. Mater.* **2017**, *29*, 1606180.

[26] H. Liang, L. Li, F. Meng, L. Dang, J. Zhuo, A. Forticaux, Z. Wang, S. Jin, *Chem. Mater.* **2015**, *27*, 5702.

[27] C. Xia, H. Liang, J. Zhu, U. Schwingenschlögl, H. N. Alshareef, *Adv. Energy Mater.* **2017**, *7*, 1602089.

[28] B. Liu, Y. F. Zhao, H. Q. Peng, Z. Y. Zhang, C. K. Sit, M. F. Yuen, T. R. Zhang, C. S. Lee, W. J. Zhang, *Adv. Mater.* **2017**, *29*, 1606521.

[29] X. Han, C. Yu, S. Zhou, C. Zhao, H. Huang, J. Yang, Z. Liu, J. Zhao, J. Qiu, *Adv. Energy Mater.* **2017**, *7*, 1602148.

[30] W. Li, X. Gao, D. Xiong, F. Wei, W.-G. Song, J. Xu, L. Liu, *Adv. Energy Mater.* **2017**, *7*, 1602579.

[31] J. Wang, L. Ji, S. Zuo, Z. Chen, *Adv. Energy Mater.* **2017**, *7*, 1700107.

[32] M. Ma, F. Qu, X. Ji, D. Liu, S. Hao, G. Du, A. M. Asiri, Y. Yao, L. Chen, X. Sun, *Small* **2017**, *13*, 1700394.

[33] M. Xie, L. Yang, Y. Ji, Z. Wang, X. Ren, Z. Liu, A. M. Asiri, X. Xiong, X. Sun, *Nanoscale* **2017**, *9*, 16612.

[34] M. Ma, G. Zhu, F. Xie, F. Qu, Z. Liu, G. Du, A. M. Asiri, Y. Yao, X. Sun, *ChemSusChem* **2017**, *10*, 3188.

[35] S. Li, S. Peng, L. Huang, X. Cui, A. M. Al-Enizi, G. Zheng, *ACS Appl. Mater. Interfaces* **2016**, *8*, 20534.

[36] O. C. Compton, A. Abouimrane, Z. An, M. J. Palmeri, L. C. Brinson, K. Amine, S. T. Nguyen, *Small* **2012**, *8*, 1110.

[37] Y. Kuang, G. Feng, P. Li, Y. Bi, Y. Li, X. Sun, *Angew. Chem., Int. Ed.* **2016**, *55*, 693.

[38] J. Wang, C. F. Tan, T. Zhu, G. W. Ho, *Angew. Chem., Int. Ed.* **2016**, *55*, 10482.

[39] X. Long, G. Li, Z. Wang, H. Zhu, T. Zhang, S. Xiao, W. Guo, S. Yang, *J. Am. Chem. Soc.* **2015**, *137*, 11900.

[40] H. Wu, M. Xu, H. Wu, J. Xu, Y. Wang, Z. Peng, G. Zheng, *J. Mater. Chem.* **2012**, *22*, 19821.

[41] J. E. Elshof, H. Yuan, P. Gonzalez Rodriguez, *Adv. Energy Mater.* **2016**, *6*, 1600355.

[42] J. Xu, J. Zhang, W. Zhang, C.-S. Lee, *Adv. Energy Mater.* **2017**, *7*, 1700571.

[43] Y. Jia, L. Zhang, G. Gao, H. Chen, B. Wang, J. Zhou, M. T. Soo, M. Hong, X. Yan, G. Qian, J. Zou, A. Du, X. Yao, *Adv. Mater.* **2017**, *29*, 1700017.

[44] M. Gao, W. Sheng, Z. Zhuang, Q. Fang, S. Gu, J. Jiang, Y. Yan, *J. Am. Chem. Soc.* **2014**, *136*, 7077.

[45] K. Xu, H. Ding, K. Jia, X. Lu, P. Chen, T. Zhou, H. Cheng, S. Liu, C. Wu, Y. Xie, *Angew. Chem., Int. Ed.* **2016**, *55*, 1710.

[46] A. J. Tkalych, K. Yu, E. A. Carter, *J. Phys. Chem. C* **2015**, *119*, 24315.

[47] H. Wu, J. Geng, H. Ge, Z. Guo, Y. Wang, G. Zheng, *Adv. Energy Mater.* **2016**, *6*, 1600794.

[48] S. Jin, *ACS Energy Lett.* **2017**, *2*, 1937.